Wu et al. Journal of the European Optical Society-Rapid Publications (2019) 15:19
https://doi.org/10.1186/s41476-019-0115-2

Journal of the European Optical Society-Rapid Publications

RESEARCH Open Access

Nano-structured transmissive spectral filter matrix based on guided-mode resonances

Wenze Wu[1,2*], Leonard Weber[1,2], Peter Hinze[3], Thomas Weimann[3], Thorsten Dziomba[3], Bernd Bodermann[3], Stefanie Kroker[2,3], Joan Daniel Prades[4], Hutomo Suryo Wasisto[1,2*] and Andreas Waag[1,2]

Abstract

Background: In this work, a nanostructured guided-mode resonance filter matrix with high transmission efficiency and narrow bandwidth is demonstrated. The developed nano-filter arrays have various usages, e.g., combined with the CMOS image sensors to realize compact spectrometers for biomedical sensing applications.

Methods: In order to optimize the filter performance, the spectral responses of filters with different structural parameters are carefully studied based on the variable-controlling method. A quality factor is carried out for quantitative characterization.

Results: In this case, a high fill factor of 0.9 can strongly suppress sidebands, while buffer layer thickness can be adjusted to mainly control the bandwidth. The transmission peaks shift from 386 nm to 1060 nm with good linearity when periods vary from 220 nm to 720 nm. The incident angle dependence is simulated to be ~ 1.1 nm/degree in ±30° range. The filters are then fabricated and characterized. The results obtained from both simulations and experiments agree well, where the filters with the period of 352 nm exhibit simulated and measured transmission peaks of 564 nm and 536 nm, the FWHM of 13 nm and 17 nm, respectively. In terms of metal material, besides aluminum, silver is also investigated towards optimization of the transmission efficiency.

Conclusion: The transmission spectra of designed filters have high transmission and low sideband; its peaks cover the whole visible and near infrared range. These characteristics allow them to have the possibility to be integrated into image sensors for spectrometer applications.

Keywords: Transmissive color filter matrix, Guided-mode resonance

Introduction

Highly compact spectrometers can be envisioned by combining CMOS image sensors with pixelwise spectral filters [1]. Ideally, the transmission function of the filter is as sharp as possible and should change from pixel to pixel, whereas the pixel distance of modern CMOS chips is in the range of a few micrometers [2, 3]. Since each pixel refers to a separate wavelength, the image of the CMOS sensor can then be transferred directly into an optical spectrum [4, 5]. In addition to the high spatial resolution [6], in order to allow e.g. multi-spectral imaging in biology, the transmission wavelength of such filters needs to be adjustable across the visible and infrared spectrum [3]. Such novel compact spectrometers will not focus on the super high resolution, but on the light information located at certain wavelengths. Some human body parameters such as blood oxygen saturation can be noninvasively determined via red and infrared light beams [7]. Other hemoglobin levels and health indicators are measurable with the same principle but using light beams at other wavelengths. Moreover, the accuracy of oxygen saturation determination can be also improved by using multispectral sensing method.

A possible realization of such a pixel spectral filter is a matrix of absorbers like organic pigments or dyes [8]. Besides the problem of depositing different dyes with micrometer resolution, those filters usually have a low transmission and a relatively broad absorption spectrum. Since they are based on organic molecules, they often suffer from degradation or aging, in particular when

* Correspondence: wenze.wu@tu-braunschweig.de; h.wasisto@tu-braunschweig.de
[1]Institute of Semiconductor Technology (IHT), Technische Universität Braunschweig, Hans-Sommer-Straße 66, 38106 Braunschweig, Germany
Full list of author information is available at the end of the article

exposed to ultraviolet radiation. In contrast to that, light can also be filtered by interference effects occurring in periodic thin film superlattices. By adjusting its parameters (e.g., layer thickness [9] or periodicity [10, 11]), the filter function of such resonant filters can be controlled. Therefore, they are now becoming more popular in various applications such as color displays [12, 13], image sensors [14], and biosensors [15]. Some dielectric nanostructure-based color printings with high spatial resolution have been reported by other groups [16, 17], but most of them work on the reflection mode, such transmissive filters are still absent.

For both chemical color filters (e.g., Bayer filters used on many commercial image sensors [18]), and resonant filters based on the variation of thin film thickness, separate photolithography steps need to be performed to laterally control the filter function. As a matter of fact, to obtain three different filter functions (i.e., for red, green and blue colors [19]), three separate photolithography steps have to be used. For spectrometers, however, the number of different wavelengths, and consequently the number of photolithography steps, is so large that this approach cannot be used. In contrast to that, filters with a lateral periodicity only require one lithography step and are thus much more convenient in terms of fabrication effort. In this case, the filter function would be controllable from pixel to pixel in a single patterning step.

There are two basic concepts for spectral filters with lateral periodicity, namely metallic nanohole array filters and guided-mode-resonance (GMR) spectral filters.

The filtering effect of arrays of nanoholes in thin metal films is due to the excitation of surface plasmon resonances (SPR) [11]. Such filters can be patterned in triangular [20] or square lattice [11, 21, 22] with different shapes of metallic holes (i.e., circular [11, 21], triangular [20], square [22] and annular holes [23]) and have been both theoretically and experimentally reported by many groups. The spectral response can be tuned by changing their lattice period. On one hand, these filters have the advantage of being fabricated by straightforward technological steps, and can then be directly integrated with image sensors. However, on the other hand, they yield low transmission efficiency, which is normally about 25–50%, with a spectral line width of the filter function (i.e., full width at half maximum (FWHM)) over 100 nm, which would be too large for a CMOS spectrometer. Yokogawa et al. have reported CMOS image sensors integrated with circular hole array color filters in different sizes from $(1 \times 1)\ \mu m^2$ to $(5 \times 5)\ \mu m^2$ [14]. Although they have realized the filter arrays with low crosstalk effect, their transmission efficiency of 40–50% could still not be further improved.

In this work, we aim at developing resonant filters based on lateral periodicity, which can be integrated into CMOS image sensors. In this case, GMR filters based on the coupling of the incident wave to an adjacent leaky lateral waveguide mode can achieve high transmission efficiency with very narrow linewidth [10]. Sharp resonance phenomena can take place only if the phases of external diffracted wave and the structural waveguide mode match. Since 1995, after Magnusson et al. introduced the first transmissive multilayer GMR filter [24], more advanced transmissive filters with various structures or thin-film materials were reported. To enhance the interaction of light and nanostructure, metal gratings are used instead of dielectric gratings in many works. The surface plasmon modes of the metal grating are excited and coupled to the waveguide mode of dielectric waveguide, that the electromagnetic field can be further extended into the waveguide [25]. However, most of these works only focus on RGB (red, green, and blue) filters [26]. Besides, those filters still have large sidebands; their bandwidth can be further optimized [27, 28]. Thus, for realizing single peak transmissive GMR filter cross whole visible and near infrared range on the micron scale with high efficiency, narrow bandwidth, and low sidebands, a comprehensive simulation of the influence of different parameters like periodicity, film thickness, and other material properties like e.g. index of refraction on the filter properties is prerequisite.

Results and discussion

To meet the desired filter requirements (i.e. high efficiency, narrow bandwidth, and low sidebands), we have chosen and designed a GMR filter architecture with metal gratings as illustrated in Fig. 1a. The design contains a low-index SiO_2 buffer layer and a high-index waveguide layer made of Si_3N_4 on top of a quartz substrate. To provide necessary lateral phase matching of an external wave to the waveguide mode, an aluminum grating on top of the buffer layer is utilized. The transmission properties of our GMR filters are determined by their structural parameters, including the fill factor (F, proportion of metal width to period), the thickness of waveguide layer (W) and buffer layer (B), the depth of metal grating (M), and grating period (P). By changing P, the transmission peaks can easily be controlled from the visible to the infrared spectral range. Figure 1b shows a simulated transmission spectrum of an aluminum-based GMR filter with parameters: $W = 100$ nm, $B = 50$ nm, $M = 30$ nm, $P = 360$ nm and $F = 0.9$. Some definitions such as the transmission peak and sideband peak amplitude, two areas surrounded by spectrum curve and x aches, as well as the FWHM are marked in the figure. The inset is the 2D schematic front view of considered filter structure with labeled structural parameters.

For the parameters optimization of the GMR filters, particularly to efficiently suppress sidebands, rigorous simulations using the commercial software tool RSoft by Synopsys

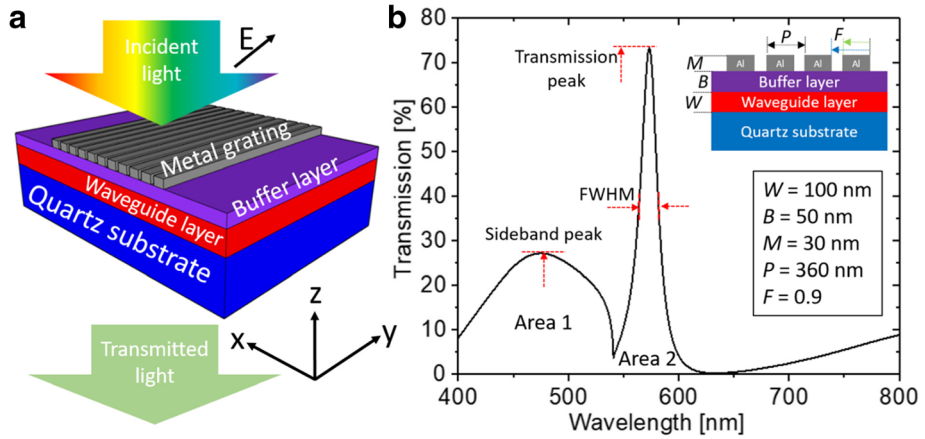

Fig. 1 **a** Schematic of the transmissive guided-mode resonance (GMR) filter structure, containing the waveguide and buffer layer on a quartz substrate. The metal gratings are located on the top. By controlling the grating periods, the peak wavelength of transmitted light spectra can be varied. **b** is a simulated filter transmission spectrum based on aluminum with defined structural parameters listed in the figure. The inset is a front view of the GMR filter

were performed. All structural parameters (i.e., *F*, *W*, *B*, *M*, and *P*) were carefully studied using the variable-controlling method, meaning that other variable predictors were held constant while the effect of changing one structure parameter was observed. All simulation spectra showed in Fig. 2 are from the filters using aluminum grating for the TM polarized light at the normal incident. The wavelengths are swept from 500 nm to 1100 nm in 5 nm steps.

To achieve a globally optimized design, the quality factor Q is defined as:

$$Q = \frac{A_2}{A_1 + A_2} \cdot (TP - SP) \cdot \frac{1}{FWHM}$$

where A_1 and A_2, TP and SP are the field area of 1 and 2, and transmission and sideband peak amplitude,

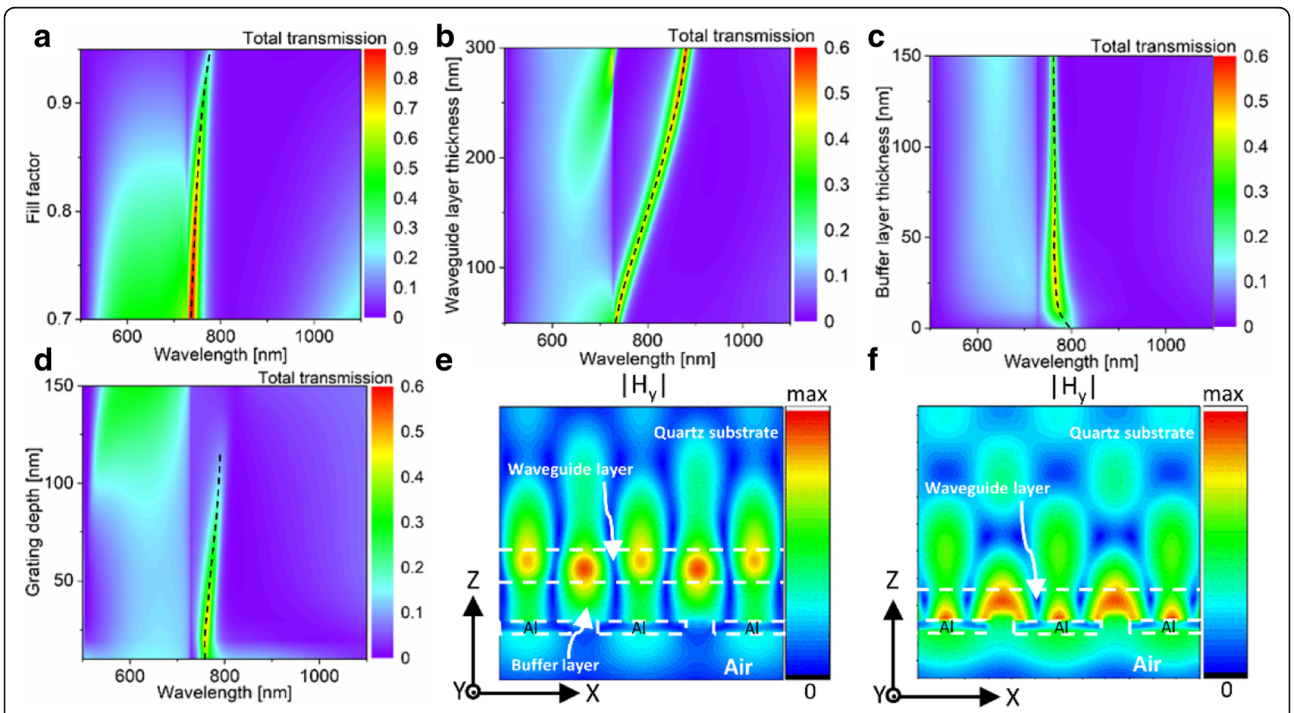

Fig. 2 Simulated transmission spectra with parameter variation of **a** fill factor from 0.7 to 0.95, **b** waveguide layer thickness from 50 nm to 300 nm, **c** buffer layer thickness from 0 (without buffer layer) to 150 nm, and **d** metal grating depth from 10 nm to 150 nm. During one parameter variation are others constant. Those original values are $P = 500$ nm, $F = 0.9$, W = 100 nm, $B = 50$ nm and $M = 30$ nm. The magnetic field distribution H_y at transmission peak wavelengths for the buffer layer thickness of 0 nm (**e**) and 150 nm (**f**)

respectively. An ideal transmission spectrum requires higher A_2 to (A_1 + A_2) ratio, a larger *TP* and *SP* difference as well as a lower *FWHM*. The largest *Q* value is searched during the whole simulation study.

At first, fill factor of the aluminum grating is varied from 0.7 to 0.95 in 0.01 steps (fill factor lower than 0.7 results even larger sideband by transmission spectrum), while other parameters were kept constant at P = 500 nm, W = 100 nm, B = 50 nm, and M = 30 nm. The simulation results are illustrated in Fig. 2a. At the maximum of the transmission peaks, a transmission of about 90% is achieved when the fill factor is lower than 0.85. But in this case, there are relatively high sidebands. Higher fill factors, equivalent to a larger fraction of the surface covered with metal, cause lower transmission but can strongly suppress the sidebands. Thus, according to the requirements of the envisioned application, the fill factor can be adjusted to obtain a suitable compromise between high transmission and low sideband contributions. In our case, for multispectral sensing applications, higher fill factor F = 0.9 was chosen for the followed studies, with peak transmission sacrifice, and lower sideband.

As shown in Fig. 2b, the transmission peak shifts from 735 nm to 882 nm when the waveguide layer thickness varies from 50 nm to 300 nm. To explain this phenomenon, we consider the eigenvalue resonance equation in such a single layer waveguide grating filters [24], which can be written as

$$\tan(k_0 p_{wi} d_w) = \frac{j p_{wi}(p_{bi} + p_{si})}{p_{wi}^2 + p_{bi} p_{si}} \quad (1)$$

where $j = (-1)^{1/2}$, $k_0 = 2\pi/\lambda$, with λ as the wavelength in free space, $p_{wi} = [\varepsilon_w - (\beta_i/k)^2]^{1/2}$, $p_{bi} = [\varepsilon_{b,eff} - (\beta_i/k)^2]^{1/2}$, and $p_{si} = [\varepsilon_s - (\beta_i/k)^2]^{1/2}$, with i as the integer number labelling the diffracted orders (i = 0, ±1, ±2, ...), ε_w, ε_s and $\varepsilon_{b,eff}$ are the relative permittivity of the waveguide layer, substrate and effective permittivity of the buffer layer with the metal grating, respectively. β_i is the propagation constant along the boundary layer. According to this equation, a larger approximate resonant wavelength λ_{res} is calculated by a thicker waveguide layer thickness d_w for a constant periodicity. A proportional relationship between center wavelength and waveguide layer thickness is also obtained from Fig. 2b, which is consistent with the equation solution. Depending on this relationship, Qian et al. have reported a tunable filter consisting of a wedge-shaped waveguide layer Ta_2O_5 with 50 nm increment of thickness resulting in a resonance peak shift from 684.2 nm to 725.3 nm [29]. The ratio of wavelength increment to thickness is much higher than our work, which is mainly because of the different waveguide material. In this work, we optimize the waveguide layer thickness of 100 nm to avoid the high sidebands at thinner or thicker waveguide layer.

The additional buffer layer in our filter design serves to reduce the bandwidth of the resonance. The buffer layer reduces the interaction of the waveguide mode with the metal grating, which causes loss. This can be observed from the 2D plot of the magnetic field distribution at transmission peak wavelengths with buffer layer thickness of 150 nm (Fig. 2e) and 0 nm (Fig. 2f). The magnetic field is no longer confined at the aluminum and dielectric layer interface when the buffer layer exists. This phenomenon is due to the presence of surface plasma mode, and the buffer layer could lead to a narrow plasmonic bandgap [30, 31]. Moreover, the transmission spectrum of the filter with ITO as buffer layer has a *FWHM* around 3 times larger than that of SiO_2 as buffer layer with the same structural parameters. The explanation is that, a more symmetry dielectric environment for the waveguide layer will be created when the buffer layer is thicker, and thus it will cause a sharper resonance. Therefore, a larger buffer layer leads to a narrower resonance bandwidth [32]. Based on this influence, we can control the filter bandwidth by tuning the buffer layer thickness. Figure 2c shows transmission spectra with buffer layer thickness ranging from 0 nm (without buffer layer) to 150 nm. As can be seen from the figure, the FWHM of the filter becomes narrower when the buffer layer thickness increases. The FWHM of a GMR filter without buffer layer is about 55 nm, which can be reduced to 25 nm when a 50 nm thick buffer layer is used.

The metal grating depth is another important parameter because of the high optical absorption of the metal. If the grating depth is varied from 10 nm to 150 nm, the transmission peak substantially reduces from 50% for the thin metal grating to almost zero, as well as the sideband develops, which is depicted in Fig. 2d. From the simulation result we can conclude that the ideal grating depth is between 20 nm and 40 nm. Lastly, the transmission spectra with optimum structural parameters and for different grating periods ranging from 220 nm to 720 nm are plotted in Fig. 3a. The transmission resonances depend on the grating periods linearly, covering the wavelengths from 386 nm to 1060 nm.

In Fig. 2a-d another interesting phenomenon can be observed: the wavelength of the main transmission peak is larger than about 730 nm mostly independent of parameter variations. This is because the corresponding wavelength range is only dependent on grating period and the material, given by the grating equation:

$$n_w \cdot \sin[\theta(i)] = n_s \cdot \sin\theta_{inc} - i\frac{\lambda}{P} \quad (2)$$

where n_w and n_s represent refractive indices of waveguide layer and substrate, respectively. θ_{inc} is the angle

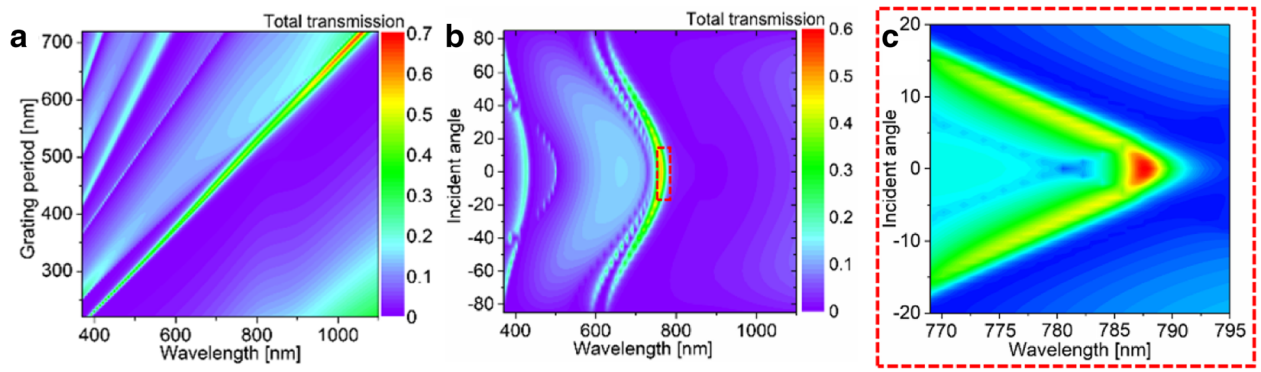

Fig. 3 **a** Transmission spectra of the GMR filter with a grating period ranging from 220 nm to 720 nm, covering the wavelengths from 386 nm to 1060 nm. **b** Angle dependence of the GMR filter with the incident angle ranging from − 85° to 85°. **c** A zoomed region from Fig (**b**) up to ±20°

of incident light, and $\theta(i)$ is the internal angle of ith order. The propagation constant along waveguide layer β can be described as

$$\beta = n_w \cdot k_0 \cdot \sin\theta(i) \tag{3}$$

By combining Eqs. (2) and (3) with the consideration of refractive index condition of total reflection in waveguide layer, we can obtain the wavelength range of allowed guided-mode resonance as

$$\max[n_b, n_w] \leq \left| n_b \cdot \sin\theta_{inc} - i\frac{\lambda}{P} \right| < n_w \tag{4}$$

with n_b as buffer layer refractive index. Thus, the minimum λ with P = 500 nm at normal incident is calculated at 730 nm, which agrees with simulated result.

Moreover, filter with the finite field (i.e., containing 5, 15, 25 or 35 grating lines) was also investigated using simulation tool. Compared with the filter with infinite gratings, the transmission spectrum of filter with only 5 gratings has two peaks instead of one single peak. A similar transmission spectrum as the infinite one (with peak shift less than 7 nm) can be achieved by filters with more than 15 grating lines.

For the optimized parameter set, the angle dependence was studied. Simulations of incident angles ranging from − 85° to 85° in 5° steps with optimized structural parameters of F = 0.9, W = 100 nm, B = 50 nm, and M = 30 nm at P = 500 nm were performed and the results are plotted in Fig. 3b. Figure 3c is the angle dependence of simulated transmission spectra up to ±20° in 1° steps. The transmission peak shifts about 34 nm if the incident angle increases from 0° to 30°, resulting in the shift rate of about 1.1 nm per degree. Consequently, for GMR filters in CMOS based spectrometers the peak wavelength shifts as a function of incident angle and has to be taken into account and the elements have to be tailored for a specific angle of incident. Normal incidence light will be mainly used in our future biomedical applications, to avoid the incident angle influences.

Moreover, as stated in some previous works [30, 31], the metal grating based GMR filter is polarization dependent. The filter matrix can be thus fabricated containing both vertical and horizontal gratings with the same periods, to compensate the polarization dependency.

The fabrication process flow for GMR spectral filters is illustrated in Fig. 4a-f. It contains the following technological steps:

(a) A 400 μm thick quartz substrate was prepared and cleaned using nitrogen gun. The first layer of waveguide was then deposited on top of the substrate by plasma enhanced chemical vapor deposition (PECVD). In this case, 100 nm thick Si_3N_4 layer was deposited within 5 min with a deposition rate of about 20 nm/min.
(b) Subsequently, a 50 nm thick SiO_2 layer was conformally applied with atomic layer deposition (ALD) technique. The SiO_2 was deposited at a temperature of 250 °C using 500 ALD cycles. Silane (SiH_4) was carried by N_2 with 1.6 s pulse time and 8 s purge time. O_2 was carried by Ar with 13.5 s pulse time and 4 s purge time. Ellipsometry (SIE EP4 LDXe+L, Accurion GmbH, Göttingen) was used to determine the layer thickness. The measured layer thickness and refractive indices of Si_3N_4 and SiO_2 layers are 84.5 nm with n ~ 2 and 49.2 nm with n ~ 1.46, respectively, which are in good agreement with literature data of refractive indices of the employed materials [33].
(c) The sample was then spin-coated using a PMMA (AR-P 671.02, Allresist GmbH, Strausberg) resist layer with a thickness of 130 nm.
(d) Afterward, the patterning step was followed using electron beam lithography tool Raith EBPG 5200 with an acceleration voltage of 100 keV and a base

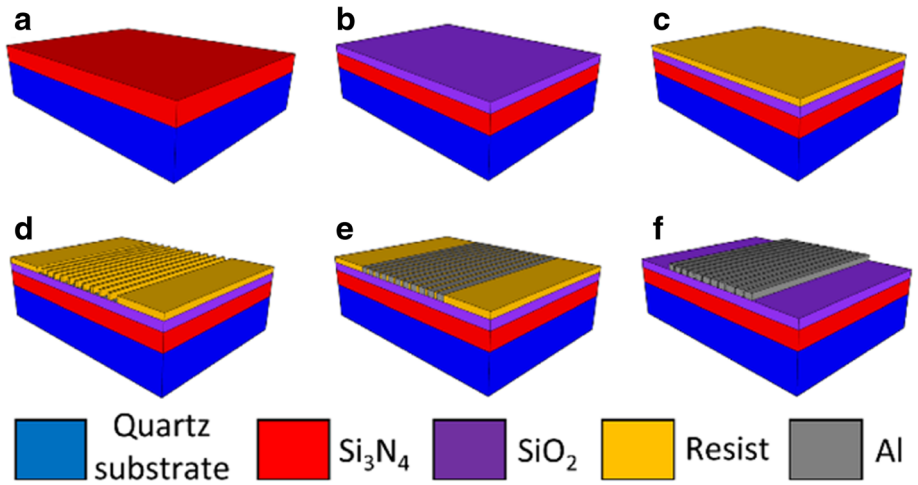

Fig. 4 Fabrication process flow of a nanofilter array based on GMR, showing the conditions of the sample after **a** substrate cleaning and plasma enhanced chemical vapour deposition (PE-ALD) of a 100 nm thick Si3N4 layer, **b** atomic layer deposition (ALD) of a 50 nm thick SiO2 layer, **c** resist coating, **d** patterning using electron beam lithography (EBL), **e** metal deposition, and **f** photoresist removal

dose of 300 μC/cm^2. The solvent of a mixture of 10 ml Methylethylketon (MEK) plus 247.5 ml Methylisobutylketon (MIBK) was used as the developer, and 742.5 ml Isopropanol (IPA) as stopper. The development and stopper (IPA) time were both 30s.

(e) A 40 nm thick aluminum layer was then deposited on the top layer.

(f) Then the sample was immerged in acetone overnight (> 12 h) for lift-off preparation. After sprayed with acetone and with IPA, blown dry with nitrogen gun, the whole nanofilter fabrication procedure ended up with photoresist removal.

The microscope image of the fabricated GMR spectral filter under white light back-illumination through a 50× objective (numerical aperture, NA, of 0.8) is shown in Fig. 5a. The sample consists of a filter matrix with cell dimensions of (9.9 × 9.9) μm^2 having grating period ranging from 360 nm to 640 nm in 20 nm steps (spread over 4 × 4 pixels), and two rectangular filters in size of 28 × 40 μm^2 with grating periods of 360 nm (green) and 600 nm (red). The bright squares in the filter matrix are the cells without metal coating. We can also observe that some filters contain black lines, which is because of the not-well-defined gratings during the fabrication process. This will be discussed in the next session. Figure 5b shows a scanning electron microscopy (SEM) image of

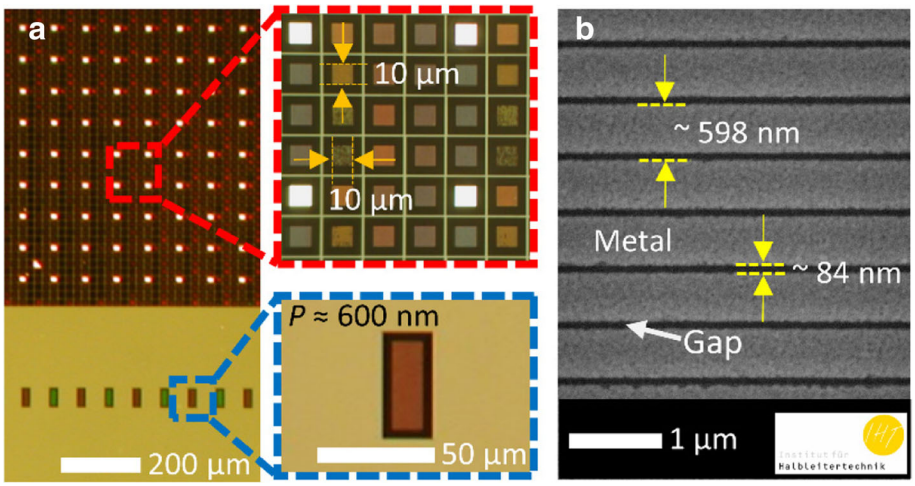

Fig. 5 a Back-illuminated microscope images of fabricated spectral filter matrix and two rectangular filters. Filter matrix comprises a hole cell without metal coating and 15 individual GMR filters with the grating period ranging from 360 nm to 640 nm in 20 nm steps. **b** SEM image of the red rectangular filter having a period of ~ 598 nm

the red rectangular filter with $P \approx 600$ nm. The structures in the SEM images with larger grating periods exhibit no defects, ensuring good color purity. The SEM measurements yield a period of (352 ± 3) nm with (52 ± 6) nm gap width ($F = 0.852$) for the green filter. Meanwhile, the red filter possesses (598 ± 7) nm period with (84 ± 5) nm gap ($F = 0.86$).

The fabricated filters were then measured by AFM (atomic force microscopy) to characterize the grating surface roughness and depth. The AFM measurements were performed with the Nanostation II non-contact AFM by SIS (Surface Imaging Systems, Germany) at PTB. A unique feature of SIS AFMs is that they use a glass fiber interferometer instead of the usual beam deflection to detect the cantilever oscillation. While beam deflection systems hardly allow any calibration of the cantilever oscillation amplitude, the glass fiber interferometers ensure a traceable measurement of the amplitude such that amplitude control can be set to optimally fit the properties of the sample under investigation. The AFM images shown in Fig. 6 were recorded with a SSS tip (SuperSharpSilicon tip by Nanosensors). The depth information is depicted by three profiles across two grooves in Fig. 6b as an example. To precisely determine the grating depth, the height histogram (i.e. the distribution of height values measured in the AFM image in the inset) for both forward and backward scan (trace and retrace) was plotted as shown in Fig. 6c. The depth of the groove was then deduced from the height difference between the centers of gravity of the two peaks: the surface of the Al shows up around 0 nm height, while a small peak at − 40 nm represents the bottom of the grating grooves, i.e. the depth of fabricated metal gratings is about 40 nm. Besides, the fabricated gratings have a V-shaped gap instead of the designed sharp edges, which is mainly because of strong proximity effect on insulating buffer layer during e-beam lithography. The AFM measured edge angle is around 77°, which is much larger than AFM tip aperture angle (22°). A cross-sectional SEM image of fabricated filter structure is depicted in Fig. 6d. As the filter structure has very thin metal layer on top of insulating substrate, this SEM image is suffering from strong charging effect. However, it can be still seen that much aluminum is attached between metal gratings, which can build such V-shaped gaps. Compared with E. Sakat *et. al*'s work [34] with similar structure but much larger period at 2100 nm, perpendicular metal gaps at sub 100 nm width on insulating substrate is really difficult to fabricate.

In order to analyze the spectral filter performance, the transmission spectra of fabricated filters were measured by a specifically designed measurement setup, which is suitable for transmission spectra measurement of such a small field area. The parallel light beam was generated via a non-polarized point light source and lenses, to illuminate individual filters controlled by a highly precise microscope. The transmitted light was then measured by a fiber spectrometer. To evaluating the filter matrix, the rectangular green filters with well-defined gaps were measured. Its transmission spectra were shown in Fig. 7. All four filters have a transmission peak of about 12.8% at 536 nm. The very similar transmission spectra show good reproducibility. Simulations with characterized structural parameters (i.e. V-shaped gaps, $F = 0.852$, $W = 84.5$ nm, $B = 49.2$ nm, $M = 40$ nm, and $P = 352$ nm) were also performed to compare with measured ones. This simulated spectrum with V-shaped gaps has a transmission reduced from 55.2% (sharp gap filter, peak at 553 nm) down to 12.6% (at 564 nm). This can be explained by the additional optical power loss at those V-shaped gaps. Nevertheless, both measured and simulated spectra agree well, have small *FWHM* of 17 nm and 13 nm, respectively. The 28 nm peak shift could be due to oxidation of metal gratings as well as high surface roughness. Higher transmission efficiency can be achieved by filters with perpendicular gap profiles, which can be fabricated by e.g., using two-step EBL. As the two-step EBL was performed with reduced beam energy in every step, this could effectively reduce the proximity effect. The optimized filter structure as well as the transmission measurement will be reported in our future work.

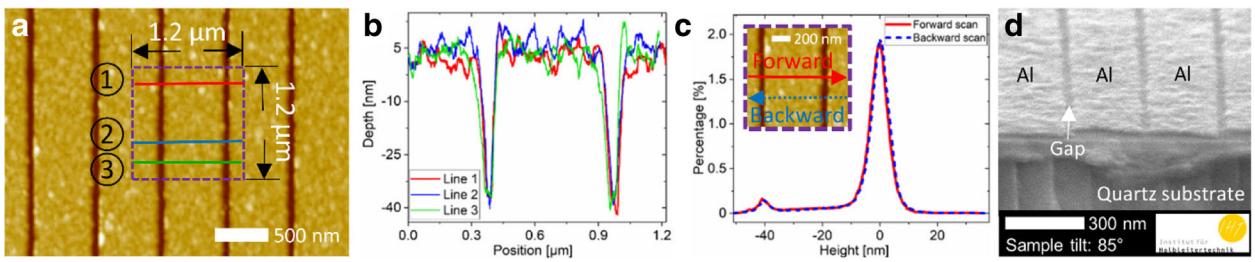

Fig. 6 **a** 3D map of rectangular filter having period of 600 nm measured with AFM, **b** depth information measured at three different positions as showed in figure (**a**), **c** percentage of different height measured with forward and backward scan, and **d** cross-sectional SEM image of fabricated grating structure

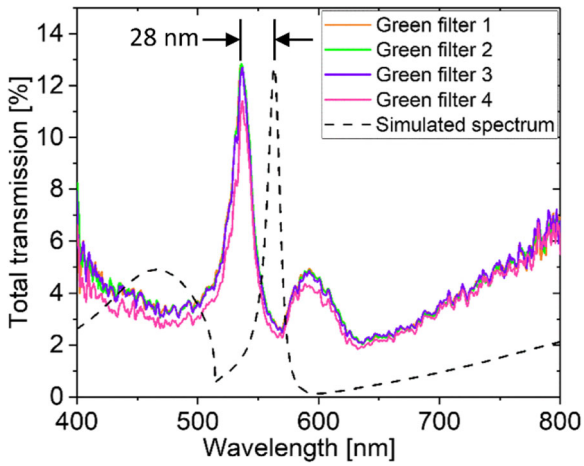

Fig. 7 Measured (colored lines) and simulated (dotted line) transmission spectra of rectangular green filters with measured structural parameters (i.e. V-shaped, $F = 0.842$, $W = 84.5$ nm, $B = 49.2$ nm, $M = 40$ nm, and $P = 352$ nm)

To investigate the enhancement feasibility of GMR filter performance, the characteristics of similar filter using other metal sets were also simulated (i.e., silver (Ag) and gold (Au)), as shown in Fig. 8. The filter using Ag instead of Al has a higher transmission even at fill factor of 0.9. However, due to worse adhesion between Ag and SiO_2 layer compared with Al, such filter could have more undesirable defects [35] and shorter lifetime. Meanwhile, normal adhesion layer used in microfabrication technique (e.g., titanium or chromium) will strongly reduce its transmission efficiency down to 20% or lower. Therefore, 5 nm thick indium tin oxide (ITO) layer as adhesion layer can be used as from the simulation results, the combination of Ag and ITO demonstrates higher transmission and lower sideband than aluminum. It thus provides a promising way for Ag-based GMR transmissive filters with high efficiency. As the ITO layer

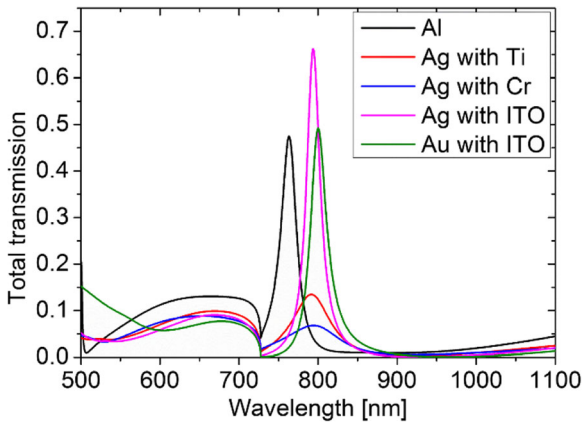

Fig. 8 Transmission spectra of GMR filter with optimized structural parameter at $P = 500$ nm and different metal gratings (i.e., Al, Ag/Ti, Ag/Cr, Ag/ITO, and Au/ITO)

is conductive, the proximity effect during EBL can also be minimized [36]. However, according to the simulation results based on different ITO layer thickness, the maximum transmission reduces to lower than 45% when the used ITO layer thickness is larger than 30 nm. As the fabrication of silver layer is not fully compatible with standard CMOS process, the experimental data for Ag based filters will be cautiously considered during the second research period in our institute.

Overall, the proposed GMR filter is able to achieve a single transmission peak instead of multi-peaks [37] over a large wavelength range. Compared with previous works [38], we use a higher fill factor to realize the low sideband spectra by reasonable scarifying the transmission efficiency, but still with narrow bandwidth. This helps our future biomedical application to collect the light information at certain wavelengths in both visible and near infrared range [4]. However, a higher fill factor means the smallest filter metal grating gap has to be fabricated down to around 30 nm in our case, which is quite challenging. This can be done by using an optimized fabrication process (e.g., two-step EBL), or other fabrication methods, (e.g., step and flash imprint lithography [38]), which will be discussed in our future work.

In our future biomedical sensing system, the filter polarization dependency can be overcome by either using a polarized light source or pattering both vertical and horizontal gratings within one matrix element. Furthermore, as mentioned previously, the minimization of filter dimension is limited by the required grating number in one filter (minimum 15 grating lines in a single filter). Thus, to integrate the filter matrix in CMOS sensors with smaller pixel size, more pixels (2×2 or 3×3 pixels) can be settled under one filter.

Conclusions

Metal-based GMR spectral nanofilters have been fabricated in size as small as (10×10) μm^2 with robust filter properties. The experimentally determined filter functions have been simulated to obtain a set of parameters like grating periods, thickness of the waveguide, buffer layer, and filling factor. The optimum parameter set is: $F = 0.9$, $W = 100$ nm, $B = 50$ nm, and $M = 30$ nm. Hence, sharp transmission functions with wavelengths in the whole visible and near IR range can be achieved. The structural parameter studies demonstrated that the position of the central transmission peak is mainly controlled by grating period, whereas the *FWHM* of the transmission peak is predominantly influenced by the buffer layer thickness. Both simulated and measured *FWHM* were under 20 nm. Moreover, simulations of GMR nanofilters with different metals indicate that silver can be more suitable than aluminum for the grating. Overall, it could be demonstrated that such GMR filters

have a very high potential to be integrated into commercial image sensors even when pixel sizes are in the order of micrometers.

Abbreviations

AFM: Atomic force microscopy; ALD: Atomic layer deposition; FWHM: Full width at half maximum; GMR: Guided-mode resonance; PECVD: Plasma enhanced chemical vapour deposition; SEM: Scanning electron microscopy; SIS: Surface imaging system; SPR: Surface plasmon resonance; SSS: Super sharp silicon

Acknowledgements

The authors thank Juliane Breitfelder, Feng Yu, Andrey Bakin, Jan Gülink, Carol Rojas-Hurtado, Peter Thiesen and Rainer Macdonald for valuable discussion and technical support. J.D. Prades acknowledges the support of the Serra Húnter program. We gratefully acknowledge the support of the Braunschweig International Graduate School of Metrology B-IGSM and the DFG Research Training Group GrK1952 "Metrology for Complex Nanosystems (NanoMet)".

Authors' contributions

WW, JDP, HSW and AW conceived and designed the simulations and experiments; WW and LW performed the simulations, WW, PH and TW manufactured the filter matrix, SK and BB designed and performed the transmission spectra measurements; TD performed the AFM measurement; WW analyzed the data; WW wrote the paper. All authors read and approved the final manuscript.

Authors' information

Not applicable.

Funding

This work is funded in part by the Lower Saxony Ministry for Science and Culture (N-MWK) within the group of "LENA-OptoSense" and in part by the European Union's Horizon 2020 research and innovation program within the project of "ChipScope – Overcoming the Limits of Diffraction with Super-Resolution Lighting on a Chip" under grant agreement no 737089.

Availability of data and materials

Not applicable.

Competing interests

The authors declare that they have no competing interests.

Author details

[1]Institute of Semiconductor Technology (IHT), Technische Universität Braunschweig, Hans-Sommer-Straße 66, 38106 Braunschweig, Germany. [2]Laboratory for Emerging Nanometrology (LENA), Technische Universität Braunschweig, Langer Kamp 6a, 38106 Braunschweig, Germany. [3]Physikalisch-Technische Bundesanstalt (PTB), Bundesallee 100, 38116 Braunschweig, Germany. [4]MIND-IN2UB, Department of Electronics and Biomedical Engineering, Universitat de Barcelona, Martí i Franquès 1, E-08028 Barcelona, Spain.

Received: 1 March 2019 Accepted: 31 July 2019
Published online: 14 August 2019

References

1. Yu, H., Han, S., Lee, J.-Y., Kim, J., Kim, Y., Arbabi, A., Shin, C., Shi, L., Arbabi, E., Kamali, S.M., Lee, H.-S., Hwang, S., Faraon, A.: Visible wavelength color filters using dielectric subwavelength gratings for backside-illuminated CMOS image sensor technologies. Nano Lett. **17**, 3159–3164 (2017)
2. Goossens, S., Navickaite, G., Monasterio, C., Gupta, S., Piqueras, J.J., Pérez, R., Burwell, G., Nikitskiy, I., Lasanta, T., Galán, T., Puma, E., Centeno, A., Pesquera, A., Zurutuza, A., Konstantatos, G., Koppens, F.: Broadband image sensor array based on graphene–CMOS integration. Nat. Photonics. **11**, 366–371 (2017)
3. Williams, C., Rughoobur, G., Flewitt, A.J., Wilkinson, T.D.: Nanostructured plasmonic metapixels. Sci. Rep. **7**, 7745 (2017)
4. Li, E., Chong, X., Ren, F., Wang, A.X.: Broadband on-chip near-infrared spectroscopy based on a plasmonic grating filter array. Opt. Lett. **41**(9), 1913–1916 (2016)
5. Burgos, S.P., Yokogawa, S., Atwater, H.A.: Color imaging via nearest neighbor hole coupling in plasmonic color filters integrated onto a complementary metal-oxide semiconductor image sensor. ACS Nano. **7**(11), 10038–10047 (2013)
6. Xu, T., Wu, Y.-K., Luo, X., Guo, L.J.: Plasmonic nanoresonators for high-resolution colour filtering and spectral imaging. Nat. Commun. **1**, 59 (2010)
7. Jubran, A.: Pulse oximetry. Crit. Care. **19**, 272 (2015)
8. Koo, H.-S., Chen, M., Pan, P.-C.: LCD-based color filter films fabricated by a pigment-based colorant photo resist inks and printing technology. Thin Solid Films. **515**, 869–901 (2006)
9. Zhang, Q., Huang, X.-G., Lin, X.-S., Tao, J., Jin, X.-P.: A subwavelength coupler-type MIM optical filter. Opt. Express. **17**, 7549–7554 (2009)
10. Wang, S.S., Magnusson, R.: Theory and applications of guided-mode resonance filters. Appl. Opt. **32**, 2606–2613 (1993)
11. Do, Y.S., Park, J.H., Hwang, B.Y., Lee, S.-M., Ju, B.-K., Choi, K.C.: Plasmonic color filter and its fabrication for large-area applications. Adv. Opt. Mater. **1**, 133–138 (2013)
12. Ko, F.-J., Shieh, H.-P.D.: High-efficiency micro-optical color filter for liquid-crystal projection system applications. Opt. Express. **39**, 1159–1163 (2000)
13. Wu, Y.-K.R., Hollowell, A.E., Zhang, C., Guo, L.J.: Angle-insensitive structural colours based on metallic nanocavities and coloured pixels beyond the diffraction limit. Sci. Rep. **3**, 1194 (2013)
14. Yokogawa, S., Burgos, S.P., Atwater, H.A.: Plasmonic color filters for CMOS image sensor applications. Nano Lett. **12**, 4349–4354 (2012)
15. Mateus, C.F.R., Huang, M.C.Y., Li, P., Cunningham, B.T., Chang-Hasnain, C.J.: Compact label-free biosensor using VCSEL-based measurement system. IEEE Photon. Technol. Lett. **6**, 1712–1714 (2004)
16. Nagasaki, Y., Suzuki, M., Takahara, J.: All-dielectric dual-color pixel with subwavelength resolution. Nano Lett. **17**, 7500–7506 (2017)
17. Dong, Z., Ho, J., Yu, Y.F., Fu, Y.H., Paniagua-Dominguez, R., Wang, S., Kuznetsov, A.I., Yang, J.K.W.: Printing beyond sRGB color Gamut by mimicking silicon nanostructures in free-space. Nano Lett. **17**, 7620–7628 (2017)
18. Lee, S.-Y., Ortega, A.: A novel approach of image compression in digital cameras with a Bayer color filter array. Image Process. **3**, 482–485 (2001)
19. Gather, M.C., Köhnen, A., Falcou, A., Becker, H., Meerholz, K.: Solution-processed full-color polymer organic light-emitting diode displays fabricated by direct photolithography. Adv. Funct. Mater. **17**, 191–200 (2007)
20. Inoue, D., Miura, A., Nomura, T., Fujikawa, H., Sato, K., Ikeda, N., Tsuya, D., Sugimoto, Y., Koide, Y.: Polarization independent visible color filter comprising an aluminum film with surface-plasmon enhanced transmission through a subwavelength array of holes. Appl. Phys. Lett. **98**, 093113 (2011)
21. Lee, H.-S., Yoon, Y.-T., Lee, S.-S., Kim, S.-H., Lee, K.-D.: Color filter based on a subwavelength patterned metal grating. Opt. Express. **15**, 15457–15463 (2007)
22. Li, W.-D., Chou, S.Y.: Solar-blind deep-UV band-pass filter (250 - 350 nm) consisting of a metal nano-grid fabricated by nanoimprint lithography. Opt. Express. **18**, 931–937 (2010)
23. Si, G., Zhao, Y., Liu, H., Teo, S., Zhang, M., Huang, T.J., Danner, A.J., Teng, J.: Annular aperture array based color filter. Appl. Phys. Lett. **99**, 033105 (2011)
24. Wang, S.S., Magnusson, R.: Multilayer waveguide-grating filters. Appl. Opt. **34**, 2414–2420 (1995)
25. Tan, C., Simonen, J., Niemi, T.: Hybrid waveguide-surface plasmon polariton modes in a guided-mode resonance grating. Opt. Commun. **285**, 4381–4386 (2012)
26. Park, C.-S., Shrestha, V.R., Lee, S.-S., Kim, E.-S.: Transmissive color switch tapping into a polarization-selective spectral filter. IEEE Photon. Technol. Lett. **26**, 12 (2014)
27. Shrestha, V.R., Park, C.-S., Lee, S.-S.: Enhancement of color saturation and color gamut enabled by a dual-band color filter exhibiting an adjustable spectral response. Opt. Express. **22**, 3691–3704 (2014)
28. Mazulquim, D.B., Lee, K.J., Yoon, J.W., Muniz, L.V., Borges, B.-H.V., Neto, L.G., Magnusson, R.: Efficient band-pass color filters enabled by resonant modes and plasmons near the Rayleigh anomaly. Opt. Express. **22**, 30843–30851 (2014)
29. Qian, L., Zhang, D., Tao, C., Hong, R., Zhuang, S.: Tunable guided-mode resonant filter with wedged waveguide layer fabricated by masked ion beam etching. Opt. Lett. **41**, 982–985 (2016)
30. Shrestha, V.R., Lee, S.-S., Kim, E.-S., Choi, D.-Y.: Polarization-tuned dynamic color filters incorporating a dielectricloaded aluminum nanowire array. Sci. Rep. **5**, 12450 (2015)

31. Koirala, I., Shrestha, V.R., Park, C.-S., Lee, S.-S., Choi, D.-Y.: Polarization-controlled broad color palette based on an ultrathin one dimensional resonant grating structure. Sci. Rep. **7**, 40073 (2017)
32. Nishihara, H., Haruna, M., Suhara, T.: Optical integrated circuits, p. 16. McGraw-Hill, New York (1989) chap. 2
33. Ikeda, K., Saperstein, R.E., Alic, N., Fainman, Y.: Thermal and Kerr nonlinear properties of plasma-deposited silicon nitride/silicon dioxide waveguides. Opt. Express. **16**, 12987–12994 (2008)
34. Sakat, E., Vincent, G., Ghenuche, P., Bardou, N., Collin, S., Pardo, F., Pelouard, J.-L., Haïdar, R.: Guided mode resonance in subwavelength metallodielectric free-standing grating for bandpass filtering. Opt. Lett. **36**, 3054–3056 (2011)
35. Kaplan, A.F., Xu, T., Guo, L.J.: High efficiency resonance-based spectrum filters with tunable transmission bandwidth fabricated using nanoimprint lithography. Appl. Phys. Lett. **99**, 143111 (2011)
36. Williams, C., Bartholomew, R., Rughoobur, G., Gordon, G.S.D., Flewitt, A.J., Wilkinson, T.D.: Fabrication of nanostructured transmissive optical devices on ITO-glass with UV1116 photoresist using high-energy electron beam lithography. Nanotechnology. **27**, 485301 (2016)
37. Hu, R., Liang, Y., Qian, S., Peng, W.: Dual-band bandpass filter based on compound metallic grating waveguide structure. Opt. Commun. **336**, 110–115 (2015)
38. Baileya, T.C., Resnickb, D.J., Mancinib, D., Nordquistb, K.J., Dauksherb, W.J., Ainleyb, E., Talinb, A., Gehoskib, K., Bakerb, J.H., Choia, B.J., Johnsona, S., Colburna, M., Meissla, M., Sreenivasana, S.V., Ekerdta, J.G., Willsona, C.G.: Template fabrication schemes for step and flash imprint lithography. Microelectron. Eng. **61–62**, 461–467 (2002)

Publisher's Note